BACHELOR'S DEGREE THESIS ON ENGINEERING PHYSICS

UNIVERSITAT POLITÈCNICA DE CATALUNYA

NICOLAUS COPERNICUS ASTRONOMICAL CENTER

Constraining the origin of the short timescales X-ray variability of the Seyfert galaxy NGC 7469

Carlos Núñez Arilla

Director

Dr. Barbara De Marco

Co-director

Dr. Jordi José Pont

Warsaw, Poland

06/2020

“Somewhere, something incredible is waiting to be known.”

-Carl Sagan

Index

List of figures

List of tables

Abstract

This bachelor's degree thesis is a small part of a much larger project related to the study of the X-ray properties of the active galactic nucleus (AGN) NGC 7469. In this report I will focus on the analysis of the short-timescales X-ray variability properties of the source, and on how these changed between epochs separated by several years.

The galaxy NGC 7469 hosts a nuclear X-ray source, powered by a supermassive black hole, characterized by flux variability on a wide range of timescales, from years down to a few hours.

I performed an extensive spectral-timing analysis of the XMM-Newton telescope observations, carried out in the years 2000, 2004, and 2015, I demonstrated, through the analysis and modelling of the fractional variability spectra of the source, that variations of the normalization of the power law and of the soft comptonization component can describe the broad shape and account for most of the observed broad X-ray band, short timescales variability. Minor residual features are observed, that might be ascribed to variability from other components (e.g. emission lines associated with a reprocessing component).

1 Introduction

The spiral type I Seyfert galaxy NGC 7469 ($z = 0.016$) is an AGN located in the constellation of Pegasus, about 200 million light years away from the Earth, with an approximate diameter of 90,000 light years and with a black hole (BH) in its centre with a mass of $1.1 \pm 0.1 \times 10^7 M_{\odot}$ [Middei *et al* 2018].

Characterized by an X-ray bright core, NGC7469 is also an infrared light source with a powerful starburst embedded into its circumnuclear region, which makes NGC 7469 a key target for study.

This source has been observed by the XMM-Newton satellite in 2000, 2004, and in 2015. It displays strong X-ray flux variability on a wide range of timescales, down to short timescales of about a few hours. The fastest variability produced by accreting BH systems is thought to be produced in the inner regions of the accretion flow. Therefore, understanding which spectral components contribute to this variability is important to understand the physical properties of the accreting gas located close to the BH.

The aim of the project is to understand which spectral components are responsible for the observed fast variability and investigate whether the X-ray variability properties of the source have changed on the time frame of 10-15 years covered by the available data sets. This will be achieved by carrying out a spectral-timing analysis of the available data sets, with focus on the modelling of the fractional root-mean-square variability spectra (F_{var}) [Vaughan *et al* 2003].

The NGC 7469 galaxy is shown in *Fig. 1.1.*

Figure 1.1: NGC 7469 (upper right) and IC 5283 (centre left) [NASA, ESA, the Hubble Heritage (STScI/AURA)-ESA/Hubble Collaboration, and A. Evans (University of Virginia, Charlottesville/NRAO/Stony Brook University)]

2 Scientific Background

2.1 Active Galactic Nuclei

An Active Galactic Nucleus (AGN) is a compact region in the centre of a galaxy whose emitted electromagnetic radiation is not due to the "normal" components of a galaxy (stars, dust, and interstellar gas). One of the main characteristics of AGN is their complex broad-band spectrum, and their high X-ray luminosity. The accretion disk (see *Fig.2.1.1*) around a supermassive BH emits thermal radiation at long wavelengths (optical/UV), thus not contributing to the X-ray emission. The observed primary X-ray continuum in these sources is instead thought to be produced via inverse Compton scattering of the thermal disk photons in a plasma of hot electrons (called “corona”), located in the very inner regions of the system, close to the supermassive BH, and with electron temperatures of the order of $100\ keV$ [Reynolds & Nowak 2003].

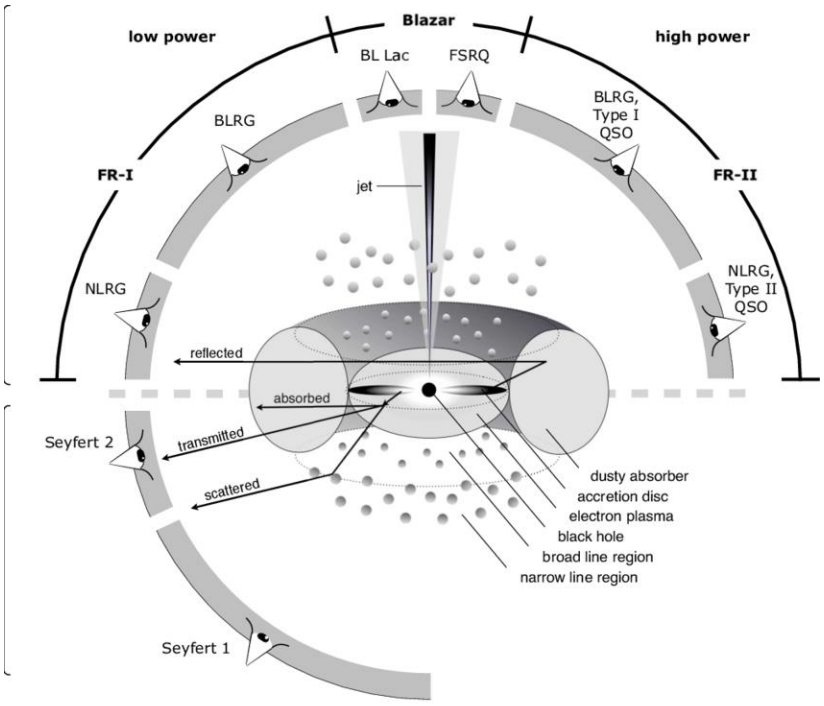

Figure 2.1.1: Schematic representation of our understanding of the AGN structure in the unified scheme [Beckmann & Shrader 2013]. NGC 7469 is a type I Seyfert galaxy, so there is no presence of relativistic jets.

This component can be phenomenologically described by a power law with a high energy cutoff (and a low energy cutoff, but this occurs at long wavelengths) as:

$$A(E) = KE^{-\alpha}\exp\left(-E/\beta\right) \qquad (1)$$

Where α is the photon index of the power law, K is the normalization of the power law and β is e-folding energy of exponential rolloff.

A fraction of the primary X-ray continuum is emitted towards the accretion disk, where it undergoes photoelectric absorption, fluorescent emission by the elements in the disk (the one with the highest fluorescence yield and abundance being iron, Fe, thus producing the strongest emission line) and a scattering continuum. Overall, these features (namely absorption edges, emission lines and a direct Compton scattering continuum) are referred to as “reflection spectrum”. If the reflection spectrum is produced by gas orbiting close to the BH (at ~ 10 gravitational radii, r_g, or below, with $r_g = \frac{GM_{BH}}{c^2}$), it is modified by relativistic effects.

Another component, whose origin is not clear, is the so-called “soft excess”. This is observed at energies below $\sim 1\ keV$, and it is characterized by an excess of emission above the extrapolated high energy power law. There is a huge debate on the origin of this component, it might be either due to a reflection component highly smeared by relativistic effects, or to a warm plasma (so-called "warm corona”) [Petrucci *et al* 2018] characterized by temperatures of a few keV and responsible for Compton up scattering the thermal photons from the disk.

2.2 X-ray variability

Another defining property of AGN is their large X-ray variability observed on a wide range of timescales (from years to minutes). All spectral components originating close to the BH should vary on short time scales (of the order of minutes-hours, but these time scales scale inversely with the BH mass [McHardy *et al* 2006]). Therefore, we can study the short time scale variability of these sources to understand the physical properties of the accreting gas (and in principle, also to derive the parameters of the BH, e.g. the mass [Ponti *et al* 2012]). For example, if the primary X-ray continuum varies and the accretion disk extends close to the BH, then also the relativistic reflection [Ross & Fabian 2015] spectrum must vary, thus contributing to the observed X-ray variability of the source. This can be used to constrain the geometry of the accretion flow.

NGC 7469 has been recently the target of a multi wavelength campaign. The X-ray data of the source show no evidence of relativistic reflection [Middei *et al* 2018], although previous analyses on Suzaku data did show some evidence of a relativistic reflection component. On the other hand, the source is highly variable on short time scales, and it shows a huge soft excess. In this project we investigated which components contribute to this short time scale variability, by analysing and modelling the so-called fractional root-mean-square variability

amplitude (F_{var}) spectrum. This spectrum shows the amount of fractional variability as a function of energy [Vaughan *et al* 2003]. This is computed from the power spectrum of the source light curve over a given range of temporal frequencies (i.e. the inverse of the timescale) of interest. Finally, the F_{var} spectrum can be modelled in order to infer which spectral components contribute to X-ray variability on the selected range of temporal frequencies [De Marco *et al* 2020].

3 Analysis

3.1 XMM-Newton

To carry out this project we used the data obtained by the X-ray Multi-mirror Mission – Newton (XMM-Newton) telescope, with the European Photon Imaging Camera (EPIC) pn (see *Fig. 3.1.1*).

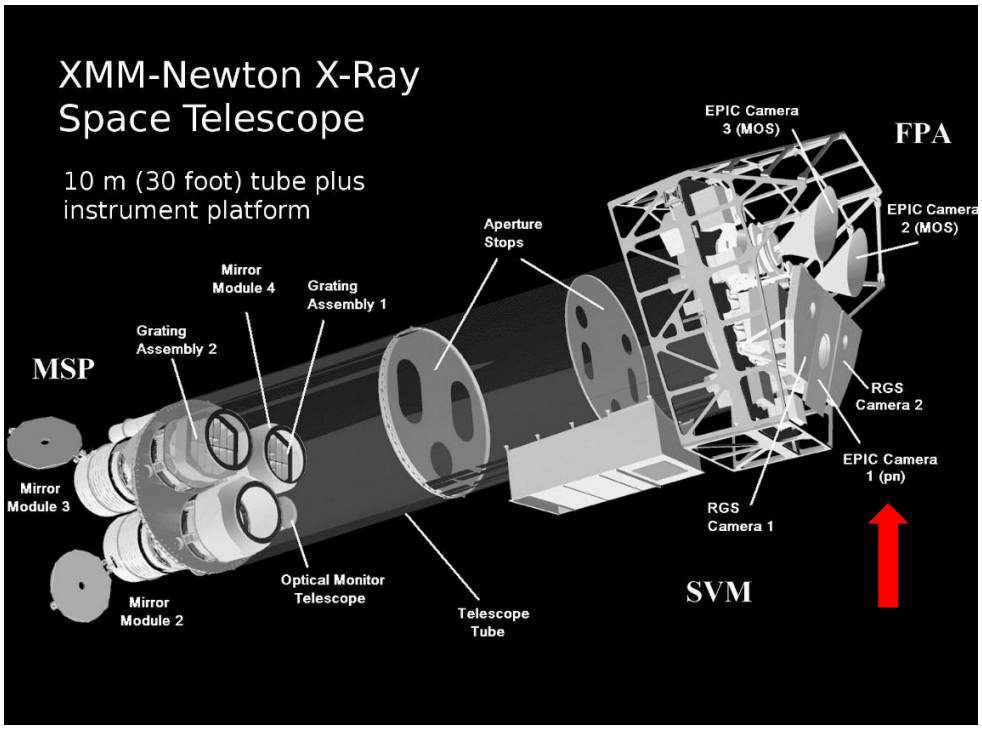

Figure 3.1.1: XMM-Newton X-ray Space Telescope scheme. (Red arrow) EPIC pn Camera

The XMM-Newton EPIC camera offers the possibility to perform extremely sensitive imaging observations over a field of view of 30 arc min and the energy range from 0.2 to $12\ keV$.

The pn camera, is formed by twelve $3 \times 1\ cm$ pn-CCDs on a single wafer (see *Fig. 3.1.2*). The four individual quadrants, each having three pn-CCD subunits with a format $200 \times 64\ pixels$, are operated in parallel.

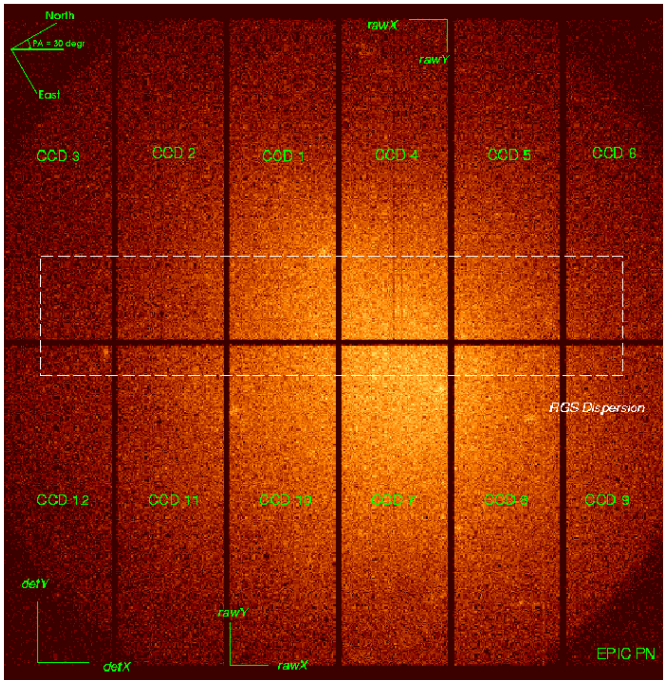

Figure 3.1.2: Scheme of the pn camera. It is a single Silicon wafer with 12 CCD chips integrated.

Among the possible observing modes, the one shown in *Fig. 3.1.3* corresponds to the SmallWindow mode, which selects only a small part of the field of view, and is the mode used during the analysed observations.

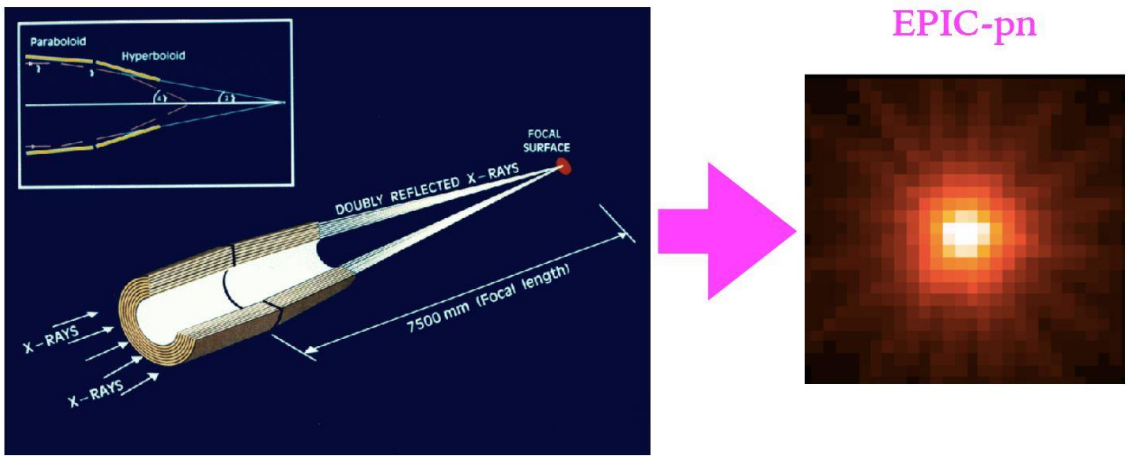

Figure 3.1.3: EPIC pn X-rays detection scheme and the image of a point source.

3.2 X-ray data cleaning and reduction

We used the observations taken by the XMM-Newton telescope in the years 2000, 2004 and 2015 (see *Table 3.2.1*).

Table 3.2.1: Log of the analysed observations. The table reports: (1) observation ID; (2) observation date; (3) net exposure time before cleaning; (4) nomenclature used throughout the paper to refer to the different datasets (the letter stands for the first number of the observation different from zero; "O" is for one, "T" is for two and "S" is for seven).

(1) ID	(2) Start Date yyyy-mm-dd hh:mm:ss	(3) Exposure [s]	(4) Obs
0112170101	2000-12-26 03:45:40	18976	O1
0112170301	2000-12-26 10:27:23	24590	O2
0207090101	2004-11-30 21:06:16	85016	T1
0207090201	2004-12-03 01:22:09	79112	T2
0760350201	2015-06-12 13:36:49	90800	S1
0760350301	2015-11-24 12:33:31	87000	S2
0760350401	2015-12-15 02:06:34	85900	S3
0760350501	2015-12-23 00:05:16	90900	S4
0760350601	2015-12-24 22:46:31	95500	S5
0760350701	2015-12-26 21:34:22	98000	S6
0760350801	2015-12-28 20:40:49	101600	S7

We carried out the data reduction using the Science Analysis System (SAS) software and updated calibration files. We created uncleaned calibrated event lists. These were filtered to obtain cleaned calibrated event lists. To this aim we first used a filter for the selection of genuine X-rays, which are identified by their PATTERN. This filter describes the type of event, namely how the charge cloud released by the infalling photon is distributed over the pixels of the detector. About two third of the EPIC pn events are single events (depending on the energy), meaning that the energy of the photon is released in one CCD pixel only. If the energy is distributed over more than one pixel, we speak of "double", "triple", etc. A good X-ray pattern must be compact, with the highest charge at the centre, and isolated (all pixels around are below threshold). We selected a PATTERN that includes single and double events, in addition, all events that were at the edge of a CCD and at the edge of a bad pixel were excluded (see *Fig. 3.2.1*).

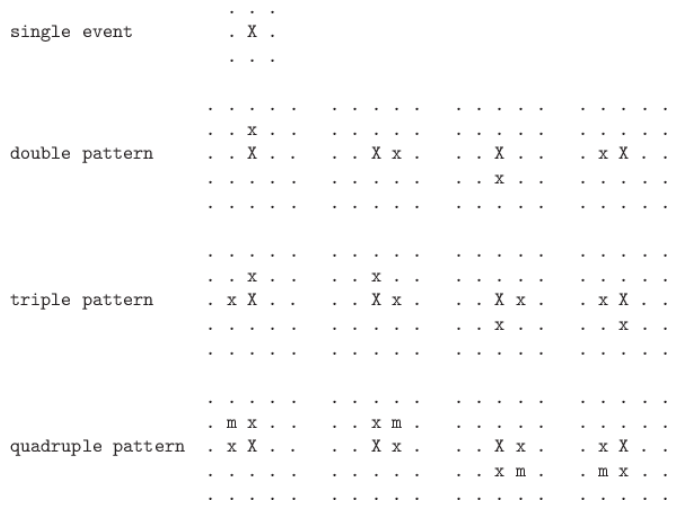

Figure 3.2.1: List of valid EPIC pn patterns. Here "." marks a pixel without an event above threshold, "X" is the pixel with the maximum charge ("main pixel"), "x" is the pixel with a non-maximum charge, "m" is the pixel with the minimum charge.

For the creation of a cleaned calibrated event list we must also filter out the background noise. We have three types of background, that related to photons, that related to particles and that related to electronic noise

The most common photons background includes: the astrophysical background from unresolved sources; the particle background associated with solar wind charge exchange and single reflections from outside the field of view, out-of-time events, etc. The particle background in particular includes: soft proton flares (i.e. particles accelerated during solar flares and hitting the detector) with spectral variations from flare to flare; internal (cosmic-ray induced) background, created directly by particles penetrating the CCDs and indirectly by the fluorescence of satellite material to which the detectors are exposed.

Thanks to PATTERN recognition, most of these background effects are filtered out, but not in the case of proton flares, whose PATTERN distribution is like that of a genuine source photon. The only solution in this case is to discard the parts of the observation most affected by these events.

To achieve this we extracted a light curve with time resolution of 1 second in the energy range $10 - 15\ keV$ (where the response of the instrument drops, so we are dominated by events that are not genuine X-rays), recognize proton flares and cut the proton flares out, by either defining a count rate threshold or a time range.

To give an example, we will use the data from observation S4. In *Fig. 3.2.2* we show the 1 second resolution light curve of the observation S4 in the $10 - 15\ keV$ energy range.

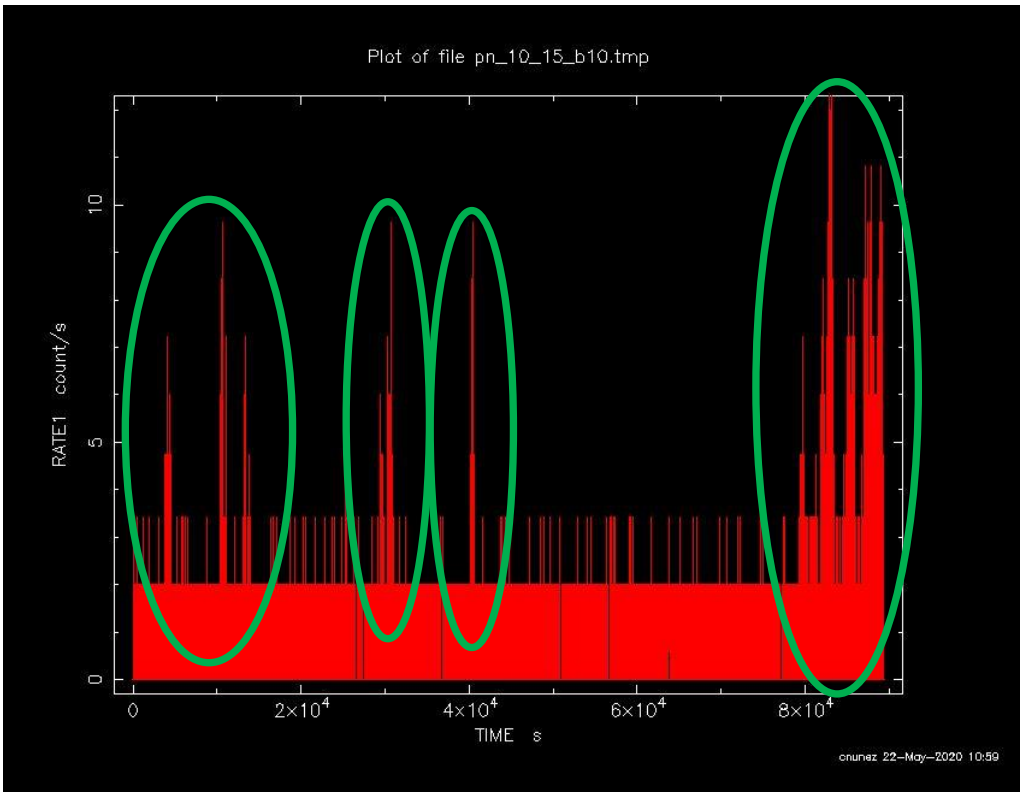

Figure 3.2.2: $\mathbf{10 - 15}\ \boldsymbol{keV}$ light curve with time resolution of 1 second of the observation 0760350501 (S4). This shows the count rate ($\boldsymbol{counts/s}$) as a function of time. The green circles mark the proton flares.

In *Fig. 3.2.3* we show the proton-flares-cleaned 1 second resolution light curve of the observation S4 in the $10 - 15\ keV$ energy range.

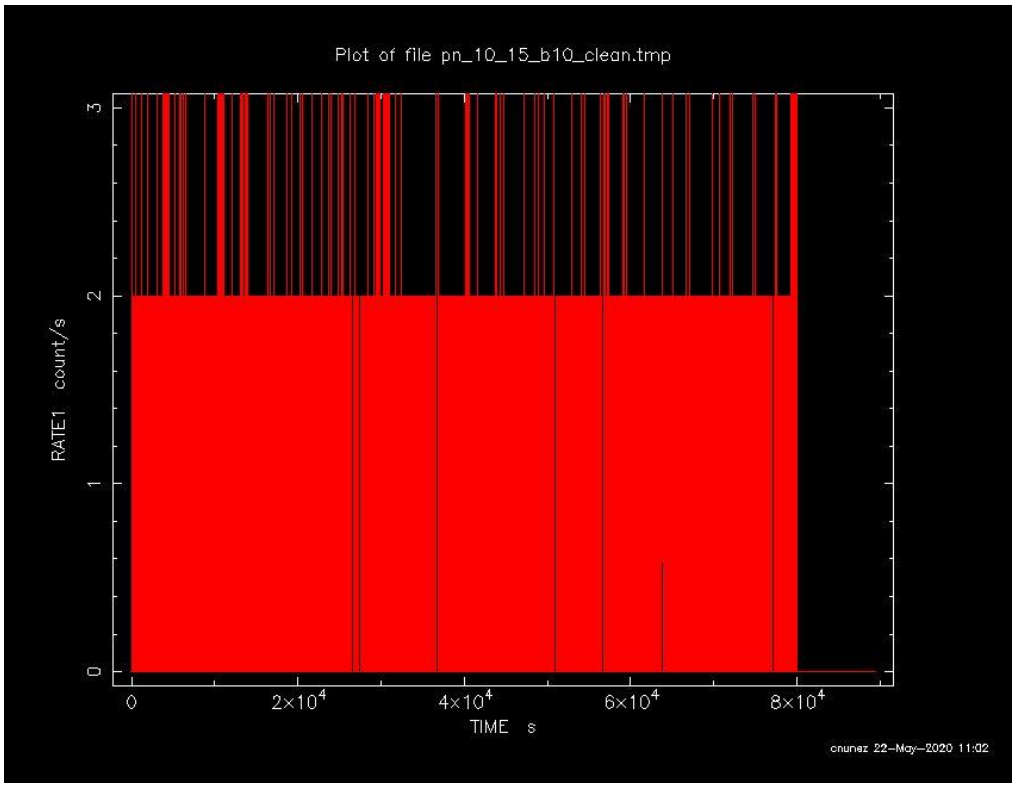

Figure 3.2.3: Cleaned $\mathbf{10 - 15}\ \boldsymbol{keV}$ light curve with time resolution of 1 second of the observation 0760350501 (S4). This shows the count rate ($\boldsymbol{counts/s}$) as a function of time. In this plot the proton flares have been filtered out.

From the cleaned event list, we extracted an image of the source and choose the source and background photons extraction regions (see *Fig. 3.2.4*).

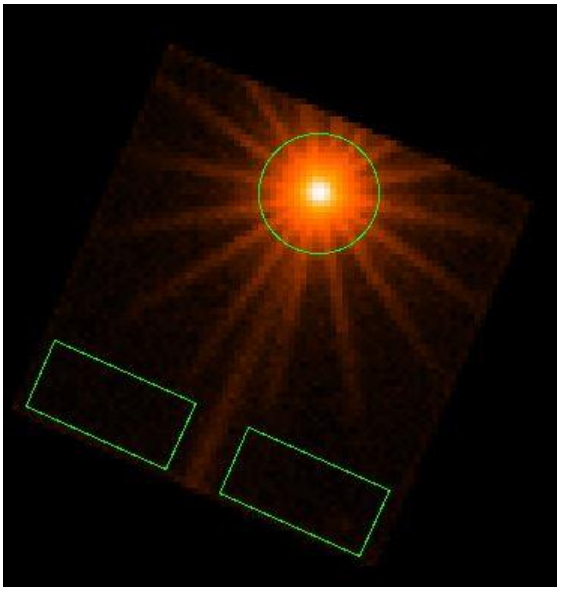

Figure 3.2.4: EPIC pn image of NGC 7469 from observation S4. The green regions show the areas chosen for the extraction of source (circle) and background (rectangles) counts. We chose two background regions to better characterize the background.

For bright sources two or more photons can deposit charge in a single pixel or in adjacent pixels during the same readout cycle. This process is called “pile-up”. The result is that we are unable to tell if there were several photons detected during this time or only one with the energy equivalent to the sum of the energies of the individual photons. As a result of pile-up, the read out electronic registers only one photon but with the energy of all involved photons. The longer the readout time and the brighter the source the larger is the chance to have pile-up.

Pile-up have some negative effects on the spectra, as the observed spectrum results harder (more hard X-ray photons and less soft X-ray photons than the real spectrum). Also, the point spread function (PSF) is influenced by pile-up, because in the core of the PSF many photons arrive at almost the same time (within one readout frame), creating multi-pixel photon patterns which are then rejected by the onboard event reconstruction, resulting in a black central point in the images.

Therefore, we checked if our observations are affected by pile-up.

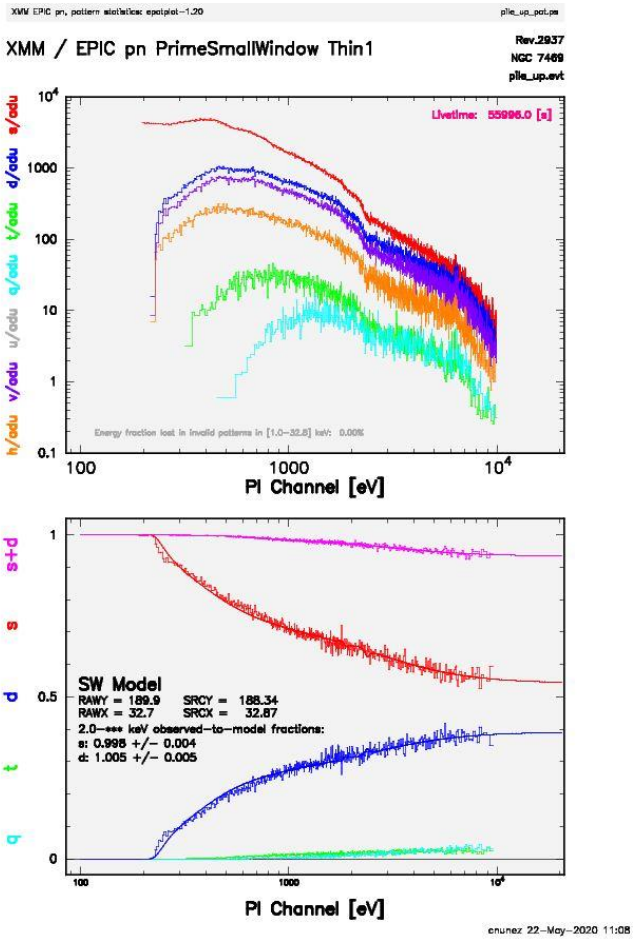

Figure 3.2.5: Pile-up spectrum of observation S4**.** The upper panel displays the spectra (distribution of counts as a function of the PI channel) of singles (red), doubles (blue), triples (green), quadruples (light blue), etc. The lower panel displays the fraction of the single, double, triple, and quadruple pattern to all events in the event file. We can see that the fraction of single events is decreasing with increasing energy. The solid coloured lines display the theoretical pattern distribution functions.

To this aim we used the SAS tool *epatplot*, which extracts the distributions of single, double, triple, etc. events and compares them to the expected distribution in the absence of pile-up (these distributions are shown in *Fig. 3.2.5*). We verified that for all the analysed observations, the observed distribution does not show significant deviations from the theoretical ones. Thus, we concluded that the level of pile-up is negligible.

This entire process of removing proton flares, extracting regions for source and background counts and checking for the possible presence of pile-up was carried out for all the observations, resulting in one cleaned and screened event file for each of them. As described in the following section, we used these files to extract light curves and spectra.

3.3 Production of X-ray light curves and spectra

We extracted background-cleaned light curves, namely the emitted counts per second as a function of time, in the energy band $0.2 - 10\ keV$ with a time resolution of 100s.

To this aim we used the SAS tools *evselect* and *epiclccorr*. The former is used to extract the light curves from the chosen source and background regions. The latter performs absolute corrections (corrections due to events lost through inefficiencies of various sorts in the mirror-detector system) and relative corrections (corrections which vary with time). Finally, this same tool is also used to rescale and subtract the background from the source light curve.

Epiclccorr also performs a correction for the dead time. The dead time is the time during each frame when the detector cannot collect photons because it is reading the previously acquired signal (so it is transferring all the charges to the reading nodes). It means that if we observe a source for 100ks a small percentage of this exposure is not used to collect photons. Accounting for dead time results in a slightly higher registered count rate, as the effective exposure time is shorter.

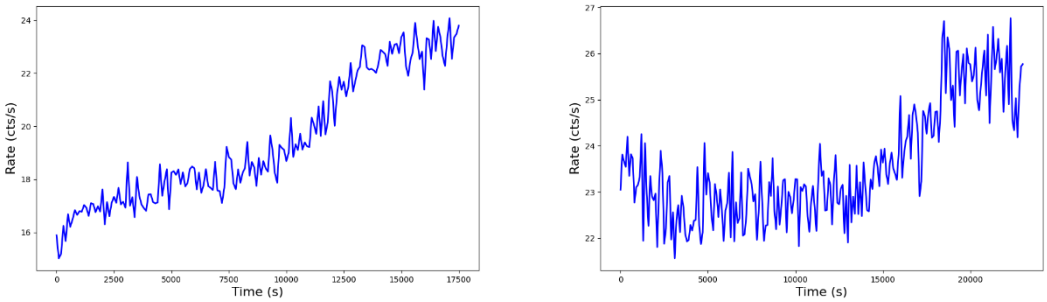

Figure 3.3.1: Light curves of observations O1 (left) and O2 (right) extracted in the energy band $\boldsymbol{0.2 - 10\ keV}$.

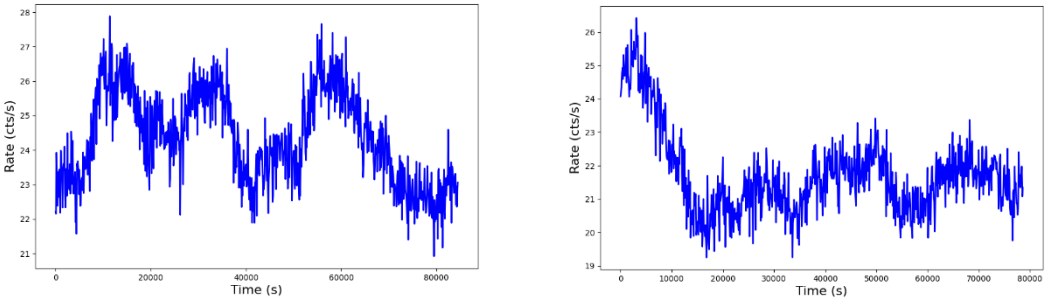

Figure 3.3.2: Light curves of observations T1 (left) and T2 (right) extracted in the energy band $\boldsymbol{0.2 - 10\ keV}$.

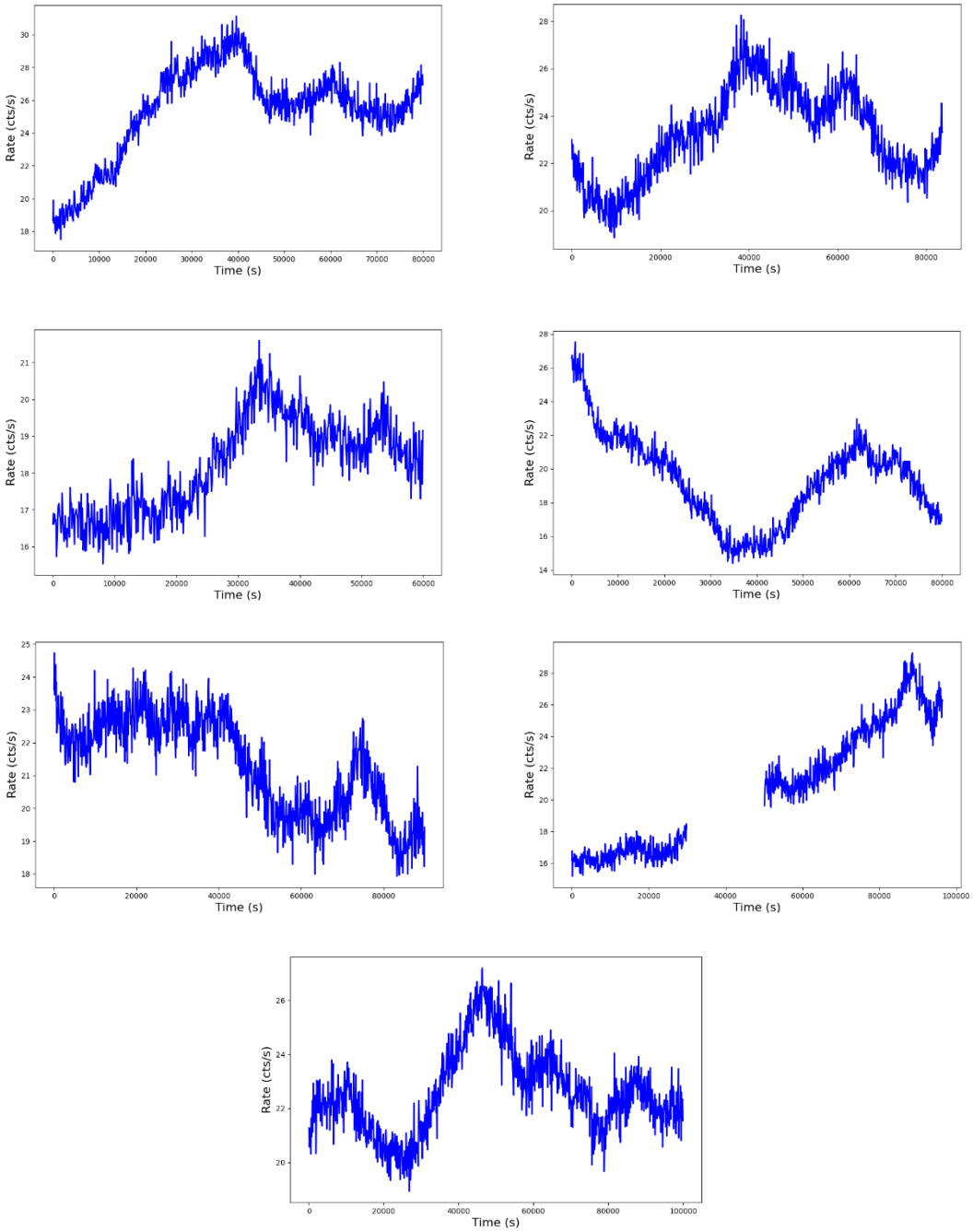

Figure 3.3.3: Light curves of the observation S1 (upper left), S2 (upper right), S3 (middle left), S4 (middle right), S5 (below left), S6 (below right) and S7 (below middle) extracted in the energy band $\mathbf{0.2 - 10}\ \boldsymbol{keV}$. Light curve of observation S6 has a gap, this is due to proton flares filtering.

The light curves of the source are shown in *Fig. 3.3.1*, *Fig. 3.3.2 and Fig. 3.3.3* As clear from these plots, the source shows remarkable variability on the sampled timescales.

We finally extracted the spectrum of the source in energy band of $0.5 - 10\ keV$, which is the energy band where the calibration of the detector is more secure. To achieve this objective, we used the SAS tools *evselect*, *backscal*, *rmfgen* and *arfgen*. The tool *evselect* is used to extract the source and background spectra. The tool *backscale* is used to calculate the areas of the

source and background extraction regions (which are then used by the fitting software to rescale the background spectrum before subtracting it from the source spectrum). The tools *rmfgen* and *arfgen* are used to compute the redistribution matrix file (a discrete function which gives the probability that an incoming photon of energy E will be detected in a channel I) and the auxiliary response file (effective area curve, which accounts for the telescope and the plus detector quantum efficiency). Finally, we rebinned the spectrum to have a minimum number of 20 photons per spectral bin for the application of χ^2 statistics.

The rebinned source spectra are shown in *Fig. 3.3.4* and *Fig.3.3.5.*

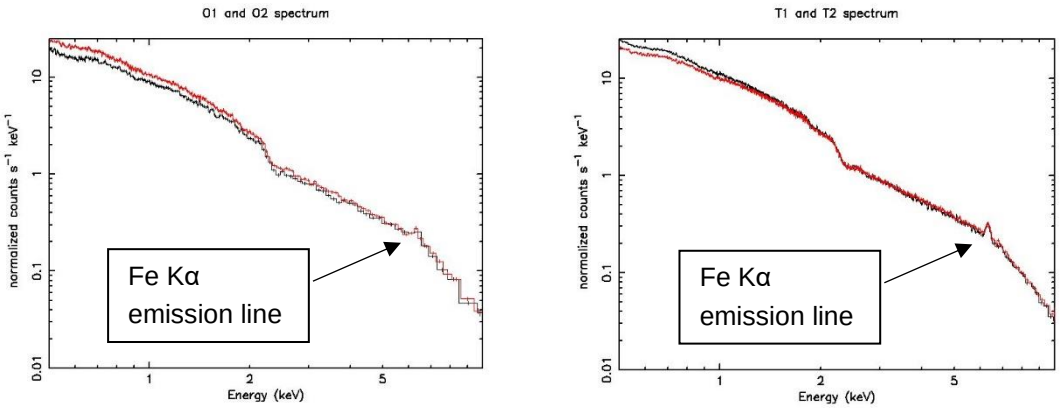

Figure 3.3.4: Source spectra of the observations (left) O1 (black) and O2 (red) and (right) T1 (black) and T2 (red). The normalized $\boldsymbol{counts\ s^{-1}\ keV^{-1}}$ are represented on the vertical axis and the energy on the horizontal axis.

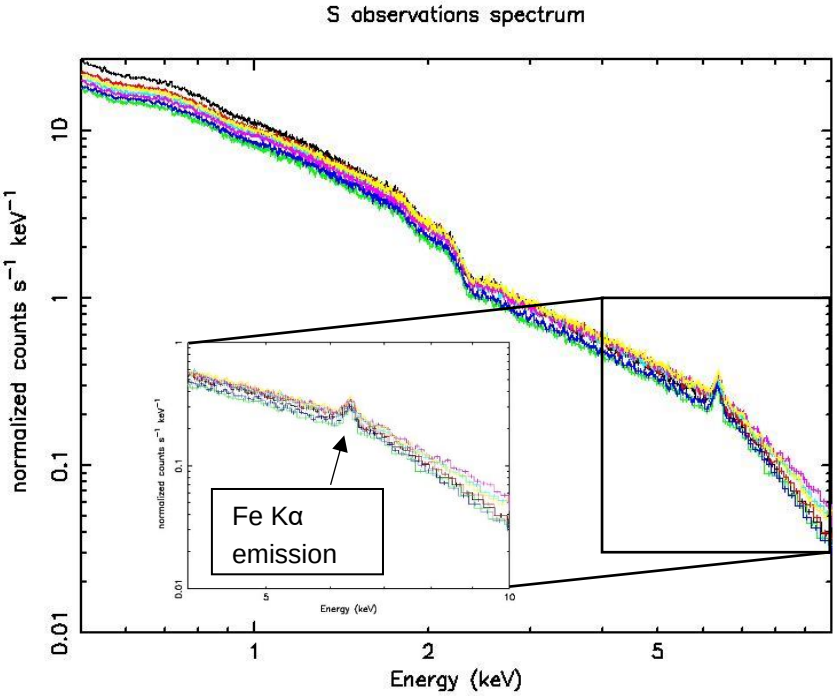

Figure 3.3.5: Source spectra of the observations S1 (black), S2 (red), S3 (green), S4 (blue), S5 (cyan), S6 (pink), and S7 (yellow).

All the spectra show a significant feature at $\sim 6.3\ keV$ associated with the neutral Fe Kα emission line (rest frame energy $6.4 keV$) [Middei *et al* 2018].

3.4 Spectral fits of time-averaged spectra

In this section we present the fits to the time-averaged spectra of all observations. The fits were performed using the X-ray spectral fitting package *Xspec*. The spectra were fit in the energy range $0.5 - 10\ keV$.

The spectra of radio quiet AGN are commonly described by the following spectral components:

- A power law (or a power law with a high energy cut off) to fit the hard X-ray continuum.
- An additional power law or a diskbb (multi-temperature black body component) component which are used to phenomenologically model the soft excess.
- A reflection component (which can be from distant gas and/or from the inner regions of the accretion disk close to the BH, see *Fig. 2.1.1*). In the latter case this component is modified by relativistic effects.

The latter are all additive components, but they are usually modified by absorption due to intervening gas, which is a multiplicative component. Absorption includes galactic absorption (due to cold gas in our galaxy lying on our line of sight to the source), but there might be also the contribution of additional absorption components which are associated with gas closer to the BH, e.g. so-called warm absorbers [Crenshaw *et al* 2003].

Therefore, we first fit the spectra of each observation using the *Xspec* model:

$$Model\ A\colon tbabs \times (powerlaw + NthComp + pexmon)$$

Where each component is as follows:

$tbabs$: Multiplicative model that represents the cold absorption column density due to the galactic medium [Wilms *et al* 2000].

$powerlaw$: Additive model that represents, as explained in *section 2.1*, a simple power law and is used here to model the hard X-ray broad band continuum.

$NthComp$: Additive model that describes thermal comptonization and is used here to model the soft excess component [Zdziarski *et al* 1996; Życki *et al* 1999].

$pexmon$: Additive model which describes neutral Compton reflection with self-consistent Fe and Ni lines [Nandra *et al* 2007; George & Fabian 1991; Matt 2002].

To determine our best-fit model we used the chi-square statistics (χ^2) [Blissett & Cruise 1979; Blissett & Kahn 1980; Loredo & Epstein 1989], defined as:

$$\chi_c^2 = \sum \frac{(O_i - E_i)^2}{E_i} \quad (2)$$

Where:

O represents the observed counts in each energy channel.

E represents the count spectrum predicted by the model.

c refers to the degrees of freedom (number of data bins minus number of model free parameters).

As our best-fit model we chose the one that minimizes the chi-square, or equivalently, the one for which $\frac{\chi^2}{c} \sim 1$, where $\frac{\chi^2}{c}$ represents the reduced χ^2.

The spectrum of observation S4 together with the residuals to the best-fit model A are shown in *Fig. 3.4.1*.

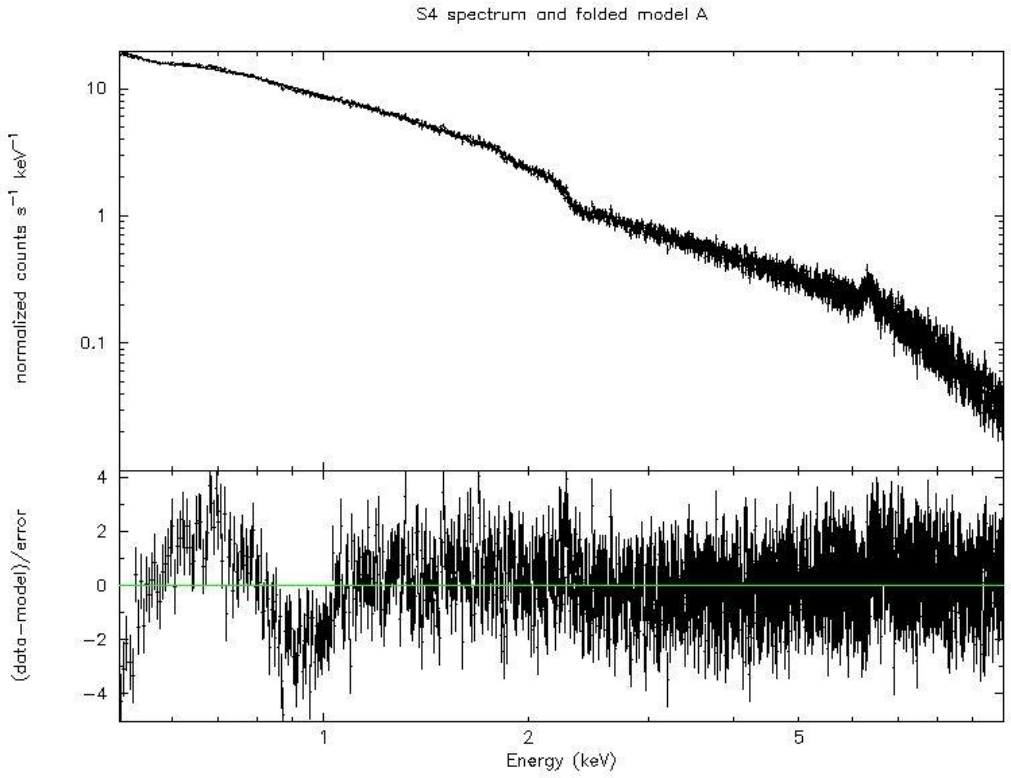

Figure 3.4.1: (Upper panel) S4 spectra, (lower panel) comparison of the data with model A. In the lower panel the residuals are plotted in terms of standard deviations from the best-fit model.

The best-fit model A yields a poor fit, with $\frac{\chi^2}{c} \sim 1.1 - 1.5$ (see *Table 3.4.1*). The best-fit parameters for model A are reported in *Table B.1*.

Table 3.4.1: Statistical results of model A.

Observation	Chi-squared	Degrees of freedom	Reduced Chi-squared
O1	1311.14	1195	1.09718
O2	1483.11	1343	1.10433
T1	2477.59	1744	1.42064
T2	2269.66	1768	1.28375
S1	2257.34	1783	1.26604
S2	2311.79	1816	1.27301
S3	1943.18	1713	1.13437
S4	2226.45	1713	1.29974
S5	2482.43	1713	1.44917
S6	2231.64	1713	1.30277
S7	2586.58	1713	1.50997

As seen in *Fig. 3.4.1* the strongest residuals are in the soft band at $E < 1.2\ keV$. We verified that this is the case for all the observations. To improve the fits, we used a more complex model.

To this aim we reproduced the model presented in Middei *et al* (2018) for S1-S7. In addition, we fit this model also to O1-O2 and T1-T2. The model is:

$$Model\ B: tbabs \times mtable\{ngc7469\_abs\} \times zashift(xillverCp + xillverCp + zgauss + gaussian + gaussian + atable\{ngc7469\_emis\} + NthComp + zgauss)$$

Where each component, except those mentioned in model A, is as follows:

$zashift$: This convolution model redshifts all additive components and is used to correct for residual calibration issues affecting the EPIC pn [Cappi *et al* 2016].

$xillverCp$: Additive reflection model used to account for both the reflection component from distant gas, and the power law describing the hard X-ray broad band continuum.

$zgauss$: A redshifted gaussian line profile. The two gaussian lines are added to account for additional emission from ionized iron and the possible presence of Nickel [Middei *et al* 2018].

$gauss$: A gaussian line profile used to correct for residual narrow features due to calibration uncertainties [Cappi *et al* 2016].

$mtable\{ngc7469\_abs\}$ and $atable\{ngc7469\_emis\}$: these are the table models, produced using the code *Cloudy* [Arav *et al* 2020], used to fit the absorption and emission components, from diffuse gas associated with the broad and narrow line regions

The energy range $2 - 2.5\ keV$ is ignored, because here the response matrix is not well calibrated, thus producing unphysical residuals [Middei *et al* 2018].

The spectrum of observation S4 together with the residuals to the best-fit model B are shown in *Fig. 3.4.2*.

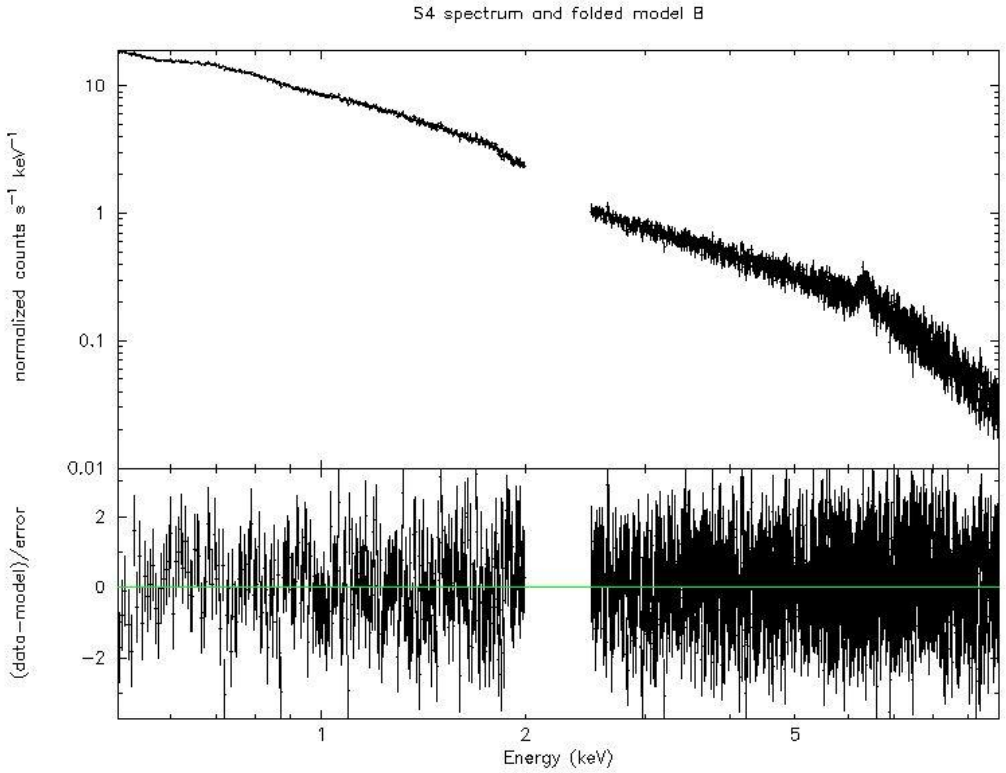

Figure 3.4.2: (Upper panel) S4 spectra without $\mathbf{2 - 2.5\ keV}$ energy range, (lower panel) comparison of the data with model B. In the lower panel the residuals are plotted in terms of standard deviations from the best-fit model.

The best-fit model B yields a better fit, with $\frac{\chi^2}{c} \sim 0.99 - 1.16$ (see *Table 3.4.2*). The best-fit parameters for model B are reported in *Table B.2*.

As seen in *Fig. 3.4.2* the residuals have decreased with respect model A. We verified that this is the case for all the observations. For this reason, we used this model for the following analysis.

Table 3.4.2: Statistical results of model B.

Observation	Chi-squared	Degrees of freedom	Reduced Chi-squared
O1	1141.05	1093	1.04396
O2	1243.58	1241	1.00208
T1	1907.89	1642	1.16193
T2	1832.37	1666	1.09986
S1	1641.66	1611	1.01903
S2	1702.87	1611	1.05703
S3	1602.11	1611	0.994482
S4	1647.43	1611	1.02261
S5	1755.83	1611	1.08990
S6	1642.55	1611	1.01958
S7	1768.26	1611	1.09762

3.5 Fractional variability spectrum

To compute the fractional rms (*root mean square*) variability spectra from the background-subtracted light curves, also called fractional variability (F_{var}) spectra [Vaughan *et al* 2003], we performed the following steps:

1. We computed the power spectrum (PSD), of the source light curves extracted in small, consecutive energy bins as:

$$P(f_j) = A\left|DFT(f_j)\right|^2 = \frac{2\Delta T}{N}\left|DFT(f_j)\right|^2 \quad (3)$$

Where DFT is the Discrete Fourier Transform of the light curve data, defined as:

$$\left|DFT(f_j)\right|^2 = \left|\sum_{i=1}^{N} x_i e^{2\pi i f_j t_i}\right|^2 = \left\{\sum_{i=1}^{N} x_i \cos(2\pi f_j t_i)\right\}^2 + \left\{\sum_{i=1}^{N} x_i \sin(2\pi f_j t_i)\right\}^2 \quad (4)$$

2. We integrated each power spectrum over a given range of frequencies:

$$S^2 = \sum_{j=1}^{N/2} P(f_j)df \quad (5)$$

Where df is the frequency resolution of the DFT ($df = \frac{1}{N\Delta T}$).

This frequency range is decided by looking at the power spectrum of the light curve in a large energy band and samples the short timescale variability of the source.

3. We used the results to compute the F_{var} spectrum. The F_{var} of each energy bin is defined as:

$$F_{var} = \sqrt{\frac{S^2 - \overline{\sigma_{err}^2}}{\bar{x}^2}} \quad (6)$$

Where $\overline{\sigma_{err}^2}$ is the mean square error due to measurement errors (Poisson noise) and $\bar{x}^2$ is the square mean of each light curve. Thus, the F_{var} represents the fraction of intrinsic source variability, in excess of statistical fluctuations due to Poisson noise.

We performed these steps using *Stingray*, a python code for timing analysis [Huppenkothen *et al* 2019].

From the background-subtracted light curves, see *section 3.3*, and using the *AveragedPowerspectrum* function, from *Stingray*, we created a PSD, *equation 3,* of the entire energy range ($0.2 - 10\ keV$), with fractional normalization . The light curve of each observation was divided into segments of equal length, the PSD computed for each segment and the resulting PSDs averaged to obtain a better estimate of the underlying PSD.

In *Fig. 3.5.1* the rebinned PSD of observations S is reported.

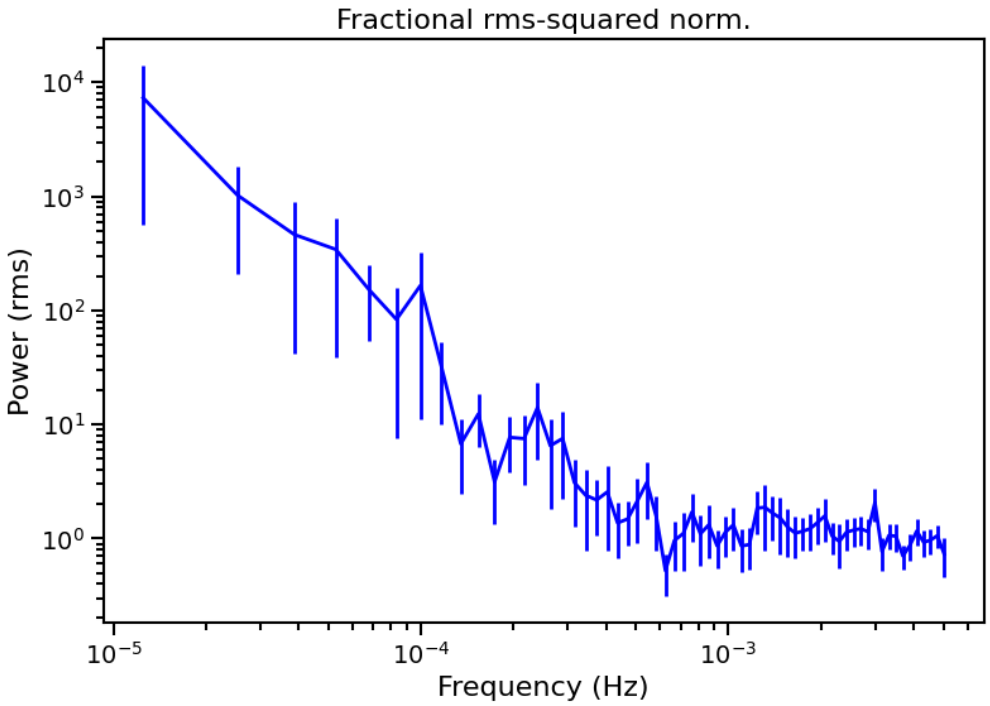

Figure 3.5.1: Rebinned PSD, with fractional rms-squared normalization, of observations S.

Above $frequency \sim 10^{-3}\ Hz$ the variability power associated with statistical fluctuations due to Poisson noise dominate. The Poisson noise has constant power at every frequency (for this reason it is also called white noise) and starts to dominate when the intrinsic variability of the source is low.

To subtract the Poisson noise and extract the intrinsic source variability power, we fit the power spectra at $frequencies > 1.5 \times 10^{-3}\ Hz$, with a constant, which allows us to determine the broad frequency band Poisson noise level (see *Fig. 3.5.2*).

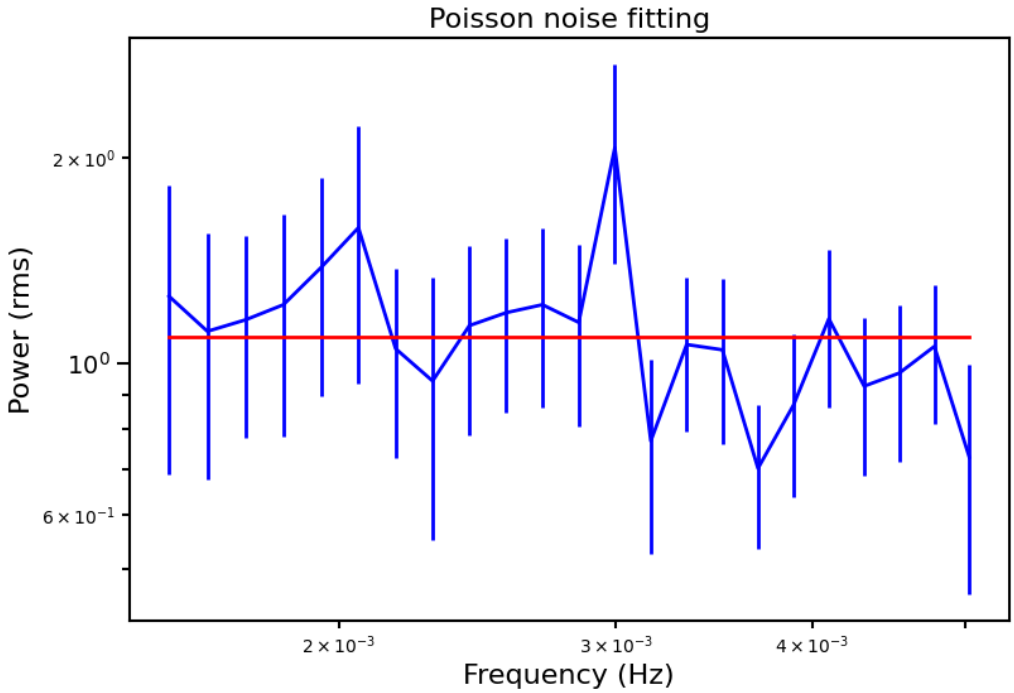

Figure 3.5.2: Poisson noise best-fit constant for observations S (red line).

We subtracted this constant value from the power at all frequencies.

We used the Poisson noise-subtracted power spectrum to infer the total fractional rms within the chosen frequency range. To this aim we integrated the power spectrum over a given range of frequencies.

To choose the frequency range, we considered two aspects:

1. For the lower limit of this range, we took the minimum value that the spectrum allows us considering that the chosen segment length. For this analysis we choose to use a segment length of 80ks, thus the minimum sampled frequency is $f_{min} = \frac{1}{80000s} = 0.125 \times 10^{-4}\ Hz$. Choosing a different segment length would allow us to extend our frequency

integration interval. However, 80ks allows us to maximize the number of averaged segments, while sampling sufficiently low frequencies.

2. Gaps in the light curves would bias the Fourier analysis. Thus, for the timing analysis, to have continuous light curves we did not filtered out short proton flares occurring in the middle of the observations. However, these may add a spurious contribution to the variability. To avoid including this contribution we chose to integrate the power spectra up to $frequencies < \frac{1}{2000s}$, since on average proton flares have a $duration <= 2ks$. Thus, the upper limit of the frequency range is $f_{max} = \frac{1}{2000s} = 0.5 \times 10^{-3}\ Hz$.

Considering the frequency range $\Delta f \sim 0.125 \times 10^{-4} - 0.5 \times 10^{-3}\ Hz$, which corresponds to timescales of twenty-two to about half an hour, we integrated the power spectrum, *equation 5*, and computed the F_{var} spectrum, *equation 6,* as:

$$F_{var} = \sqrt{\sum_{\Delta f} PSD_{clean}^{i} df} \tag{7}$$

Where i indicates the power spectrum values within the range of frequencies of interest, df is the length of each frequency bin and is equal to $\frac{1}{80000} Hz$.

The errors on the F_{var} spectrum, *equation 7,* are computed following Arévalo *et al* (2008).

$$dF_{var} = \frac{1}{2 \cdot F_{var}} \sqrt{\frac{{rms_n}^2 + 2 \cdot rms_n \cdot {F_{var}}^2}{N}} \tag{8}$$

Where:

dF_{var} is the error on the fractional rms.

rms_n is the fractional rms of the Poisson noise component, within the frequency interval we use to compute the fractional rms. Since the power spectrum of the Poisson noise component is constant over frequency, rms_n is just the product of the best-fit Poisson noise level times the width of the integration frequency interval.

N is the product of the number of light curve segments we averaged over times the number of original frequencies contained in the frequency interval we integrate the power spectrum over.

The power spectrum of the total energy band was used to define the frequency interval of interest and to illustrate the overall procedure. Consequently, we applied this procedure to the power spectra of smaller energy bins, to compute an F_{var} spectrum.

To this aim, we developed python scripts which allowed us to automatized the procedure in order to compute light curves in each energy bin, then their power spectrum, subtract the Poisson noise, integrate each Poisson noise-corrected power spectrum and use that value to construct the F_{var} spectrum.

3.6 Constructing the F_{var} spectrum

We discarded observations O1, O2, S3 and S6. Indeed, observations O1, O2 and S3 have a too short net exposure which does not allow us to sample frequencies as short as $\frac{1}{80000} Hz$. For the same reason we ignored observation S6, given the gap in the data after filtering of proton flares (*see Fig. 3.2.3*)

We computed two F_{var} spectrum, one for observations T (T1, T2) and the second for observations S (S1, S2, S4, S5, S7) thus allowing us to study the short timescales variability of the source during two different epochs separated by about 11 years.

The F_{var} spectrum of observations T is shown in *Fig. 3.6.1.*

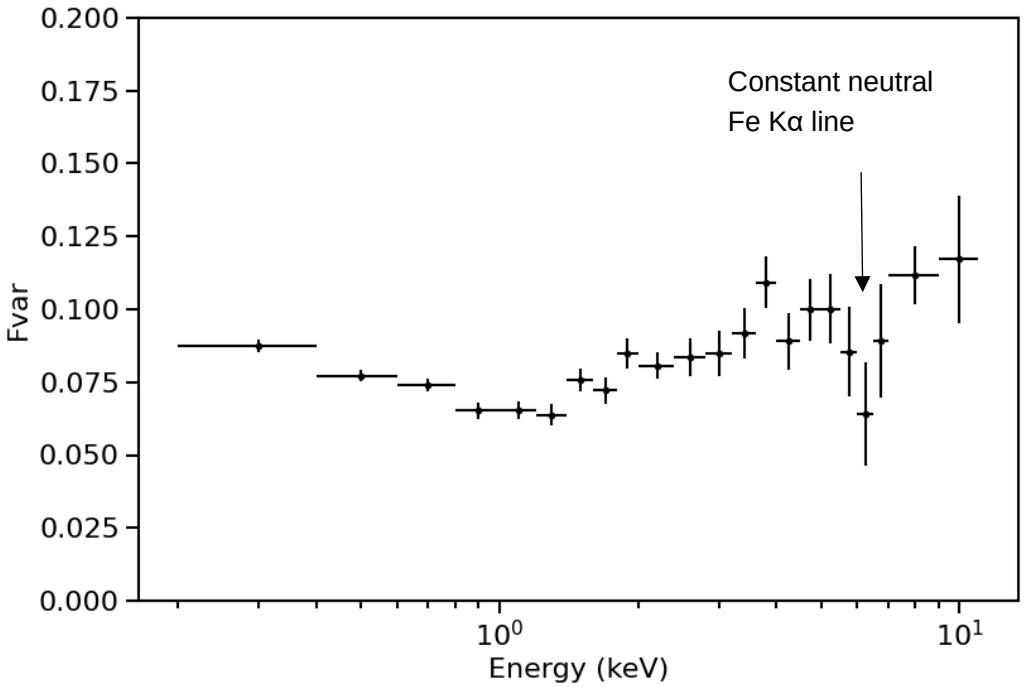

Figure 3.6.1: Fractional variability spectrum of the observations T1 and T2.

The F_{var} spectrum of observations S is shown in *Fig. 3.6.2.*

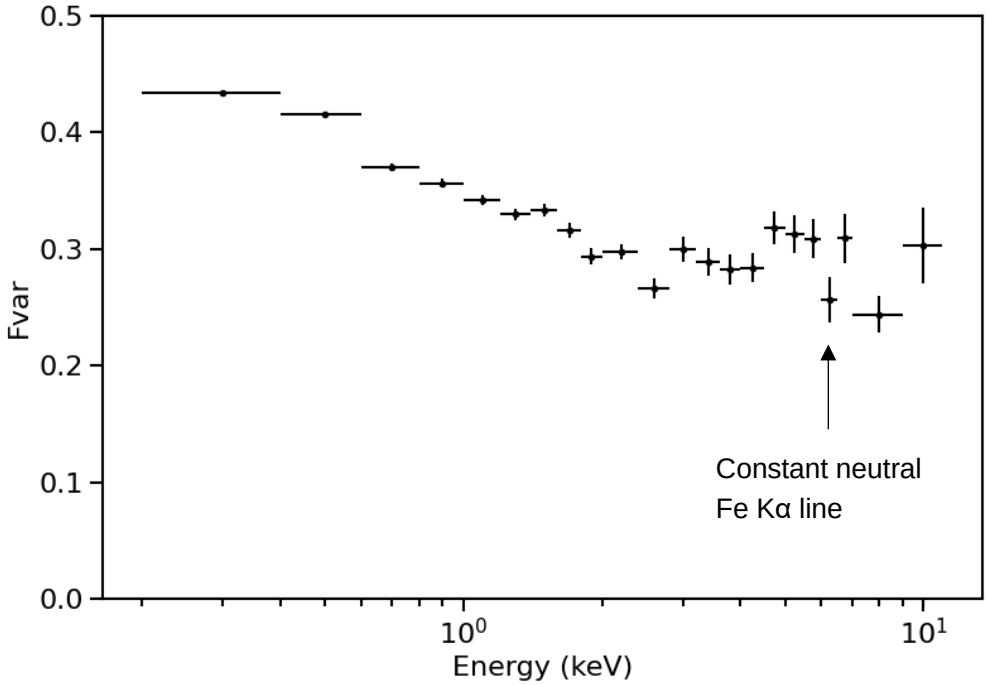

Figure 3.6.2: Fractional variability spectrum of the observations S1-S7 excluding observations S3 and S6.

The width of the energy bins is chosen to obtain good S/N. The higher energy bins are wider, to counteract the decrease of photon counts at these energies.

The two F_{var} spectrum show significant spectral variability within each epoch as well as between the two epochs. In both cases a drop is seen at $\sim 6.3\ keV$, this is due to the narrow neutral Fe Kα line, which has a rest frame energy of $6.4\ keV$. The drop indicates the neutral Fe Kα line is constant on the sampled short timescales.

3.7 Modelling of the F_{var} spectrum

We modelled the F_{var} spectrum to reproduce the observed shape assuming the best-fit spectral model B described in *section 3.4* [De Marco *et al* 2020].

For the modelling we simulated F_{var} spectra assuming that a single or more parameters of a given component of the best-fit spectral model vary on short timescales.

We found that the model that best describes the observed F_{var} spectrum includes a power law and a soft Comptonization component varying in normalization (then "*norm*" parameter of the xillverCp and nthComp components in *Table B.2*). To obtain this model we let the normalization of these two components vary following a log-normal distribution centred on their best-fit value (as commonly seen in AGN) [Uttley *et al* 2005]. We randomized the log of the norm, and then our new value for the normalization is the exponential of the result of this randomization:

$$PN = e^{(log_e(p)+\sigma \cdot ran)} \quad (9)$$

Where:

PN is the new value for the parameter.

ran is a random number extracted from a Gaussian distribution centered at zero and with standard deviation $\sigma = 1$.

σ is the assumed standard deviation of the log-normal distribution.

p is the best-fit value of the parameter (see *Table B.2*).

The width of the distribution determines the variability amplitude of each spectral parameter (see *Fig. 3.7.1*).

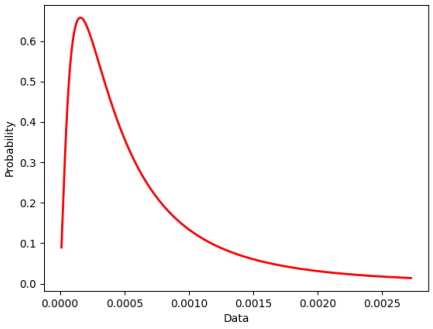

Figure 3.7.1: Log-normal probability distribution of the xillverCp *norm*.

We adjusted the sigma σ of the distribution so as to obtain the models that qualitatively better describe the observed F_{var} spectrum.

A comparison between the theoretical model and the data of T1 and T2 observations is shown in *Fig. 3.7.2*.

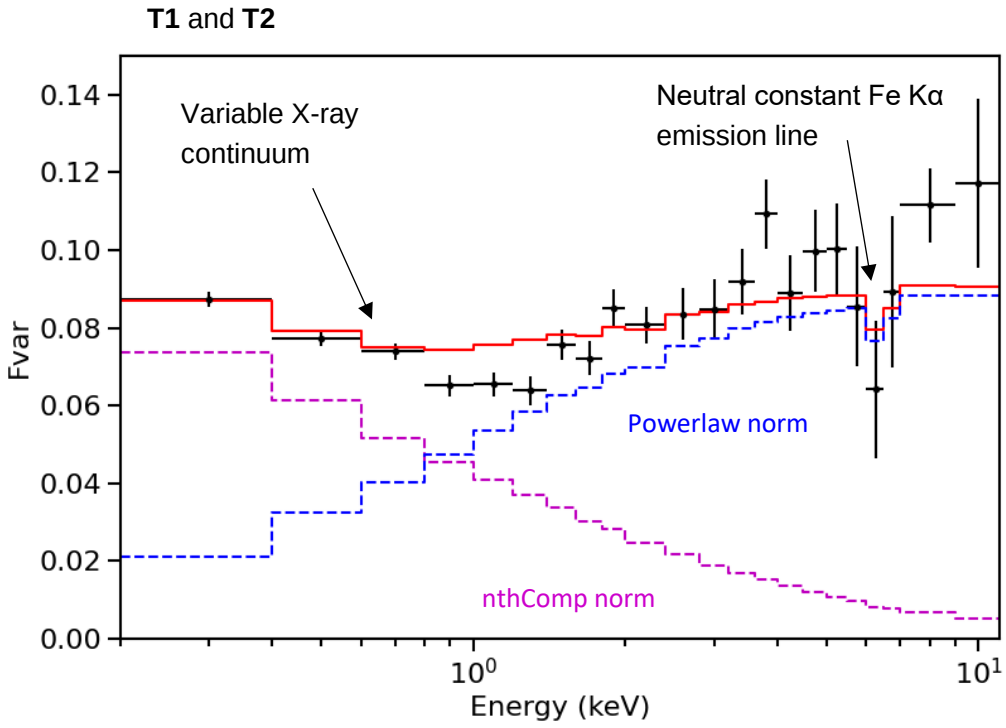

Figure 3.7.2: The Fvar spectrum of observations T1-T2 and the model that better describes it. The blue dashed line is the Fvar model produced by variations of the power law normalization only. The dashed magenta line is the Fvar model produced by variations of the normalization of the soft Comptonization component only. The red line is the model resulting from letting the two parameters vary simultaneously.

For observations T1 and T2, the theoretical model describes the data quite well. We calculated that the maximum deviation between the model and the data is $\sim 20\%$ in the soft energy range and $\sim 24\%$ in the high energy range.

In the energy range $1 - 2\ keV$ and in the high energy range $> \sim 8\ keV$ the model respectively overestimates and underestimates the observed variability. This may be indicative of more complexities that are missed in the current modelling. We discussed this in *section 4*.

A comparison between the theoretical model and the data of observations S is shown in *Fig. 3.7.3*.

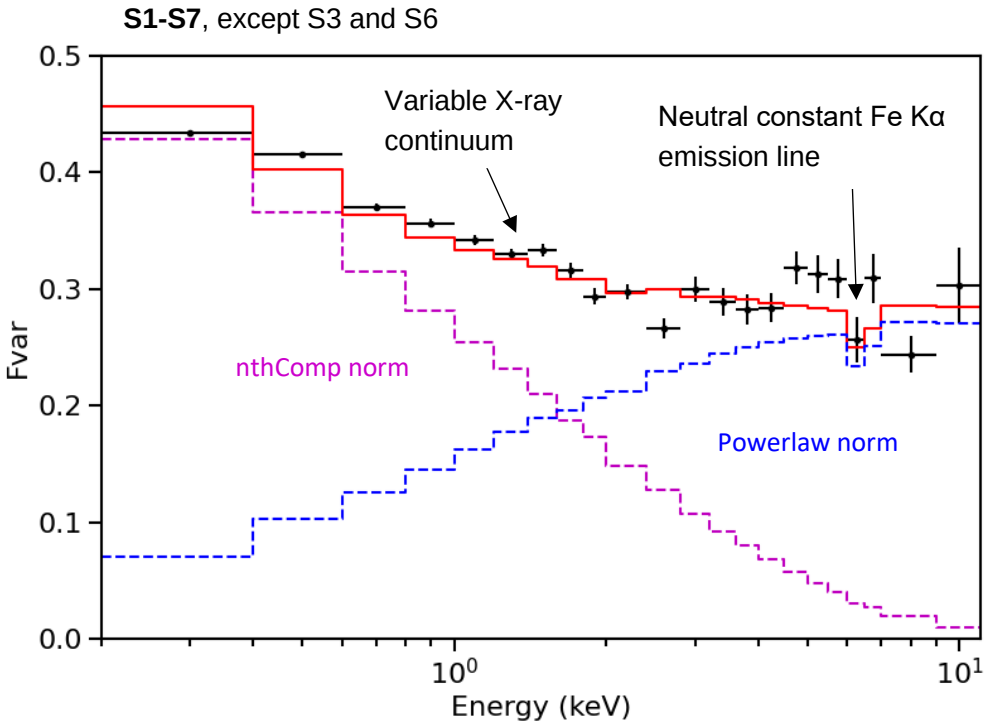

Figure 3.7.3: The Fvar spectrum of observations S and the model that better describes it. The blue dashed line is the Fvar model produced by variations of the power law normalization only. The dashed magenta line is the Fvar model produced by variations of the normalization of the soft Comptonization component only. The red line is the model resulting from letting the two parameters vary simultaneously.

For the observations S the theoretical model describes the observed F_{var} spectrum better. Agreement between the F_{var} model and the data is found deviations of maximum $\sim 5\%$ in the soft energy range and $\sim 17\%$ in the high energy range.

The model very well describes the constant emission due to the Fe Kα line, but excess variability is observed red- and blue-ward of the line.

These are the models that best describe the data among those checked. In *Appendix A* we report the models obtained assuming variable: 1) powerlaw spectral index and normalization, and 2) soft Comptonization normalization and powerlaw spectral index. These, however, show large discrepancies with the data.

4 Results and Discussion

Our results show that variations of the soft excess and hard X-ray continuum normalization are likely responsible for most of the observed short timescale variability of NGC 7469. This behaviour is quite common in Seyfert I AGN, where the soft excess is seen to contribute similar amounts of short timescale variability as the hard X-ray power law [Ponti *et al* 2012]. Moreover, the short-sampled timescales indicate an origin in the inner regions, supporting the general idea that the soft excess is produced in the inner parts of the accretion flow. While mild spectral variations of the power law index cannot be excluded, they do not seem to contribute significantly. We also note that our simple F_{var} model over/underestimates the data in narrow energy ranges, especially close to the Fe Kα line. This might indicate contribution from additional components, e.g. the excess residuals redward of the Fe Kα line in *Fig. 3.7.3* might be suggestive of a relativistic component not clearly seen in the time-averaged spectrum.

The other tested models (*Appendix A*) do not reproduce the data as well.

A more rigorous approach would be to develop an automatized procedure which is able to systematically test for variability of more parameters simultaneously and over a wider range of fractional variability. This would imply also to systematically perform goodness-of-fit tests for each model, so as to find the one that best describes the data from a statistical point of view.

To know if the degree of variability of the light curves have changed between the years of the observations, we must consider the red noise fluctuations of the light curves. Our errors on the F_{var} include only the Poisson noise contribution, but the stochastic nature of the process we are measuring is such that stronger fluctuations due to red noise can contribute to this uncertainty. We did not estimate the uncertainties due to red noise because they are not relevant for the modelling of the F_{var} spectra (they are relevant only for the overall normalization of the F_{var} spectrum). But to compare the F_{var} between two epochs and say whether the source was more or less variable in the past, we must take into account also this uncertainty. To do that we need to better constrain the underlying power spectrum of the source [Vaughan *et al* 2003].

5 Conclusions and Perspectives

The short time scale variability of the source can be qualitatively explained in terms of variations of the normalization of the power law and of the soft comptonization component. Minor residual features are observed, that might be ascribed to variability from other components (e.g. emission lines associated with a reprocessing component) and a fit with more complex models would be needed.

Interestingly, the source short timescale X-ray variability properties do not seem to have drastically changed over the timespan of about 11 years.

The work discussed in this report is part of a larger project aimed at studying the X-ray properties of NGC 7469. This source has extensive multiwavelength coverage, thus allowing the contribution from different spectral components at various distances from the central BH to be studied.

6 Acknowledgments

This project shows how extensive and varied the world of astrophysics is, combining many disciplines such as statistics, particle physics or relativity. This project started out as an idea to make and delve into the world of BH and everything that surrounds them, in this case, the accretion disk and the X-rays that emerge from it and we have ended up obtaining results from which we can find important conclusions.

To carry out this bachelor's degree thesis, I have required the help of many people, both academically and personally.

For the first I would like to thank Dr. Barbara De Marco and her PhD student Marta Dziełak for granting me the opportunity to carry out this exciting project and for the help I have received in learning a new programming language as well as entering this world. For my four-months visit to the N. Copernicus Astronomical Center PAN I acknowledge local financial support through the European Union's Horizon 2020 research and innovation programme under the Marie Skłodowska-Curie grant agreement No. 798726.

Next, I would like to thank Dr. Jordi José Pont for instructing me on this journey and in moments of despair to find a place in his agenda to find what has become of this work. And finally, to Mr. Lazaro for guiding me during the decision-making process, without him I surely would not have been able to do the Erasmus.

And on a personal level, I would like to thank my family for all their financial and emotional support during this experience, which for reasons beyond our control has sometimes been complicated. Without all these people this journey would not have been possible.

From all my heart. Thank you.

7 References

- Arav N., Xu X., Kriss G.A., Chamberlain C., Miller T., Behar E., Kaastra J.S., Ely J.C., Peretz U., Mehdipour M., Branduardi-Raymont G., Bianchi S., Cappi M., Costantini E., De Marco B., di Gesu L., Ebrero J., Kaspi S., Middei R., Petrucci P.-O. & Ponti G., *Multi-wavelength campaign on NGC 7469 V. Analysis of the HST/COS observations: Super solar metallicity, distance, and trough variation models*, A&A 633, A61 (2020)
- Arévalo P., Uttley P., Kaspi S., Breedt E., Lira P. & McHardy I. M., *Correlated X-ray/optical variability in the quasar MR 2251−178*, Monthly Notices of the Royal Astronomical Society, Volume 389, Issue 3, p. 1479-1488. (2008)
- Beckmann V. & Shrade C. R., *The AGN phenomenon: open issues*, arXiv:1302.1397 (astro-ph) (2013)
- Blissett R. J., & Cruise A. M., *The restoration of astronomical X-ray spectra,* Monthly Notices of the Royal Astronomical Society, vol. 186, p. 45-57. (1979)
- Blissett R. J., & Kahn S. M., *The direct deconvolution of X-ray spectra,* Astrophysical Journal, Part 1, vol. 238, May 15, 1980, p. 417-431. (1980)
- Cappi M., De Marco B., Ponti G., Ursini F., Petrucci P. O., Bianchi S., Kaastra J. S., Kriss G. A., Mehdipour M., Whewell M., Arav N., Behar E., Boissay R., Branduardi-Raymont G., Costantini E., Ebrero J., Di Gesu L., Harrison F. A., Kaspi S., Matt G., Paltani S., Peterson B. M., Steenbrugge K. C., and Walton D. J., *Anatomy of the AGN in NGC 5548,* A&A 592, A27. (2016)
- Crenshaw D. M., Kraemer S. B., Gabel J. R., Kaastra J. S., Steenbrugge K. C., Brinkman A. C., Dunn J. P., George I. M., Liedahl D. A., Paerels F. B. S., Turner T. J. & Yaqoob T., *Simultaneous Ultraviolet and X-Ray Spectroscopy of the Seyfert 1 Galaxy NGC 5548. I. Physical Conditions in the Ultraviolet Absorbers,* The Astrophysical Journal, 594, p.116-127. (2003)
- De Marco B., Adhikari T. P., Ponti G., Bianchi S., Kriss G. A., Arav N., Behar E., Branduardi-Raymont G., Cappi M., Costantini E., Costanzo D.,

di Gesu L., Ebrero J., Kaastra J. S., Kaspi S., Mao J., Markowitz A., Matt G., Mehdipour M., Middei R., Paltani S., Petrucci P. O., Pinto C., Różańska A., & Walton D. J., *Incoherent fast variability of X-ray obscurers. The case of NGC 3783*, A&A 634, A65 (2020)

- George I. M., & Fabian A. C., *X-ray reflection from cold matter in Active Galactic Nuclei and X-ray binaries,* Monthly Notices of the Royal Astronomical Society, Vol. 249, 352. (1991)
- Huppenkothen D., Bachetti M., Stevens A. L., Migliari S., Balm P., Hammad O., Khan U. M., Mishra H., Rashid H., Sharma S., Evandro Martinez Ribeiro E. & Valles Blanco R., *Stingray: A Modern Python Library for Spectral Timing,* The Astrophysical Journal, v.881, 39. (2019)
- Loredo T. J., & Epstein R. I., *Analyzing Gamma-Ray Burst Spectral Data*, Astrophysical Journal v.336, p.896 (1989)
- Matt G., *The iron Kα Compton shoulder in transmitted and reflected spectra*, Monthly Notice of the Royal Astronomical Society, Volume 337, Issue 1, pp. 147-150. (2002)
- McHardy I. M., Koerding E., Knigge C., Uttley P. & Fender R. P., *Active galactic nuclei as scaled-up Galactic black holes*, Nature 444, 730–732. (2006)
- Middei R., Bianchi S., Cappi M., Petrucci P. O., Ursini F., Arav N., Behar E., Branduardi-Raymont G., Costantini E., De Marco B., Di Gesu L., Ebrero J., Kaastra J., Kaspi S., Kriss G. A., Mao J., Mehdipour M., Paltani S., Peretz U. & Ponti G. *Multi-wavelength campaign on NCG 7469 IV. The broad-band X-ray spectrum.* A&A, 615. A163. (2018)
- Nandra K., O'Neill P. M., George I. M., & Reeves J. N., *An XMM-Newton survey of broad iron lines in Seyfert galaxies*, Monthly Notices of the Royal Astronomical Society, Volume 382, Issue 1, pp. 194-228. (2007)
- Petrucci P. O., Ursini F., De Rosa A., Bianchi S., Cappi M., Matt G., Dadina M., & Malzac J., *Testing warm Comptonization models for the origin of the soft X-ray excess in AGNs,* A&A 611, A59. (2018)
- Ponti G., Papadakis I., Bianchi S., Guainazzi M., Matt G., Uttley P., & Bonilla N. F*., CAIXA: a catalogue of AGN in the XMM-Newton archive III. Excess variance analysis,* A&A 542, A83. (2012)
- Reynolds C. S. & Nowak M. A., *Fluorescent iron lines as a probe of astrophysical black hole systems*, Physics Reports, Volume 377, Issue 6, p. 389-466. (2003)
- Ross R. R. & Fabian A. C., *A comprehensive range of X-ray ionized-reflection models*, Monthly Notices of the Royal Astronomical Society, Volume 358, Issue 1, p. 211-216. (2015)

- Uttley P., McHardy I. M. & Vaughan S., *Non-linear X-ray variability in X-ray binaries and active galaxies*, Monthly Notices of the Royal Astronomical Society, Volume 359, Issue 1, May 2005, p. 345–362. (2005)
- Vaughan S., Edelson R., Warwick R. S. & Uttley P, *On characterizing the variability properties of X-ray light curves from active galaxies*, Monthly Notices of the Royal Astronomical Society, Volume 345, Issue 4, p. 1271-1284. (2003)
- Wilms J., Allen A., & McCray R., *On the Absorption of X-Rays in the Interstellar Medium*, The Astrophysical Journal, Volume 542, Issue 2, p. 914-924. (2000)
- Zdziarski A. A., Johnson W. N., & Magdziarz P., *Broad-band γ-ray and X-ray spectra of NGC 4151 and their implications for physical processes and geometry,* Monthly Notices of the Royal Astronomical Society, Vol. Vol. 283, No. 1, p. 193-206. (1996)
- Życki P. T., Done C., & Smith D. A., *The 1989 May outburst of the soft X-ray transient GS 2023+338 (V404 Cyg)*, Monthly Notices of the Royal Astronomical Society, Volume 309, Issue 3, p. 561-575. (1999)

Appendix A: F_{var} models

We tested models of variations of the power law spectral index. We assumed it varies following a Gaussian distribution.

We first let the spectral index vary (green dashed line, assuming a pivot point at $\sim 3.5\ keV$) together with the normalization of the powerlaw, which is assumed to vary following a log-normal distribution, *equation 9*, (blue dashed line). See *Fig. A.1* and *Fig. A.2.*

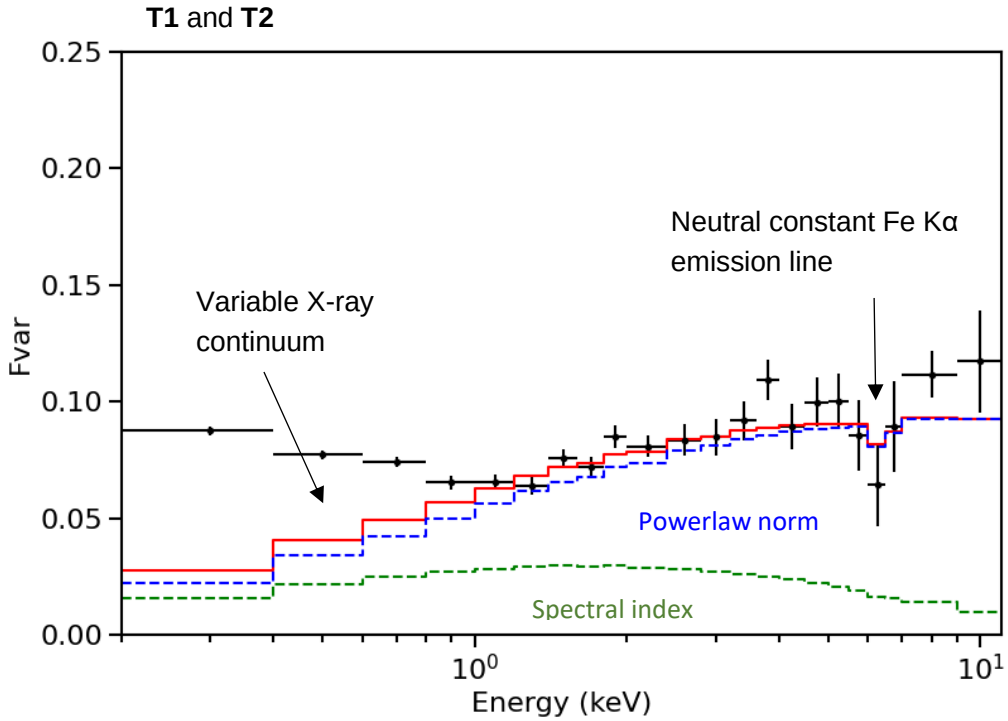

Figure A.1: The Fvar spectrum of observations T1-T2 and the tested model (I). The blue dashed line is the Fvar model produced by variations of the power law normalization only. The dashed green line is the Fvar model produced by variations of the power law spectral index only. The red line is the model resulting from letting the two parameters vary simultaneously.

The theoretical model does not describe the data in the soft excess region, reaching extremely high deviations, up to $\sim 66\%$. This model reproduces the hard energy range well, where the variability drop due to the Fe Kα emission line appears.

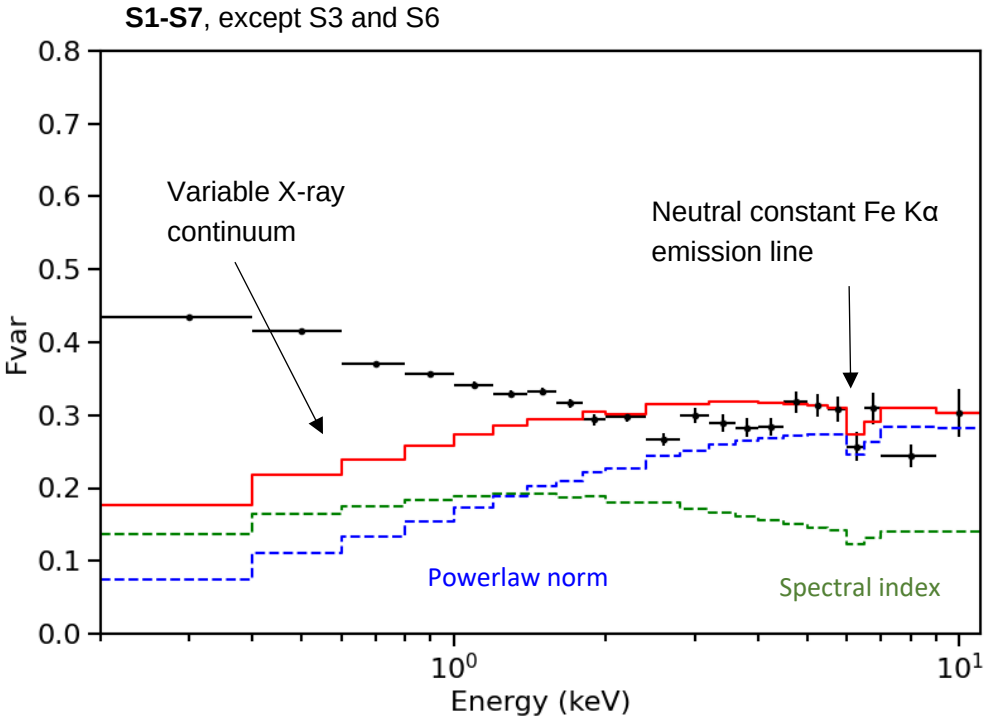

Figure A.2: The Fvar spectrum of observations S and the tested model (I). The blue dashed line is the Fvar model produced by variations of the power law normalization only. The dashed green line is the Fvar model produced by variations of the power law spectral index only. The red line is the model resulting from letting the two parameters vary simultaneously.

For the observations S, the theoretical model fails to reproduce the data in the soft excess band too. Reaching deviations of the order of $\sim 58\%$. This model fits very well in the hard energy range $E \gtrsim 5\ keV$, where the variability drop due to the Fe Kα emission line is visible.

We then tried to let the normalization of the soft Comptonization component vary (following a log-normal distribution, *equation 9*, magenta dashed line) together with the spectral index of the power law (green dashed line). See *Fig. A.3* and *Fig. A.4.*

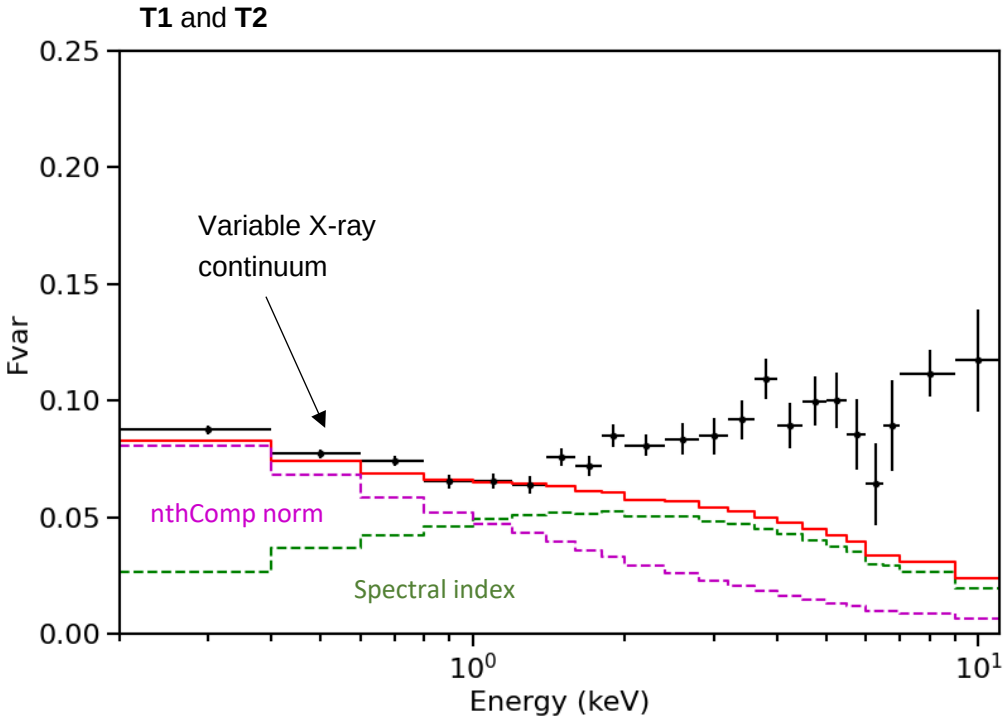

Figure A.3: The Fvar spectrum of observations T1-T2 and the tested model (II). The green dashed line is the Fvar model produced by variations of the power law spectral index only. The dashed magenta line is the Fvar model produced by variations of the normalization of the soft Comptonization component only. The red line is the model resulting from letting the two parameters vary simultaneously.

The theoretical model (red line) does not reproduce the data in the hard energy range $E \gtrsim 1.5\ keV$, reaching extremely high deviations (more than 100%). This model fits well in the soft energy range, being extremely accurate in the $\sim 0.8 - 1.5\ keV$ range.

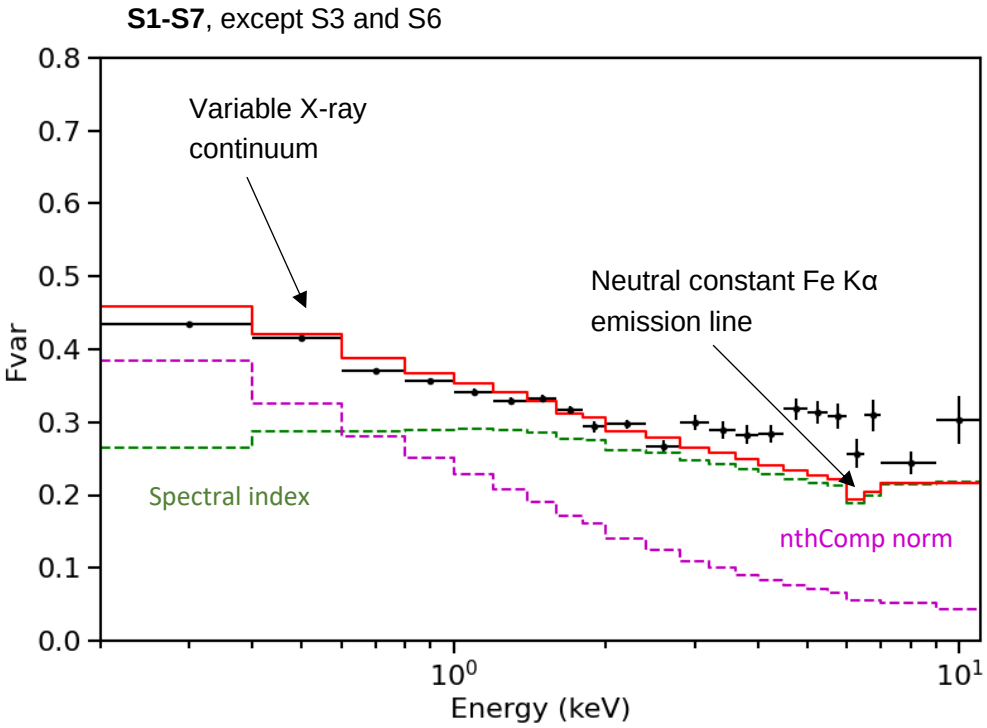

Figure A.4: The Fvar spectrum of observations S and the tested model (II). The green dashed line is the Fvar model produced by variations of the power law spectral index only. The dashed magenta line is the Fvar model produced by variations of the normalization of the soft Comptonization component only. The red line is the model resulting from letting the two parameters vary simultaneously.

Also, for observations S, the theoretical model fails to reproduce the data in the hard energy range $E \gtrsim 3\ keV$, reaching high deviations ($\sim 32\%$). This model describes the data well in the energy $\sim 0.2 - 3\ keV$ range.

Appendix B: Model parameters tables

The parameters that are not frozen are those that can vary during the fitting process.

Table B.1: Parameters of the best-fit model A of the observation S4

Model	Parameter	Value	Error (+/-)	Unit
TBabs	*nH*	4.480E-02	frozen	$10^{22}\ cm^{-2}$
powerlaw	*PhoIndex (p2)*	1.823	1.165E-02	
	norm	7.532E-03	1.350E-04	
nthComp	*Gamma*	3.363	8.936E-02	
	kT_e	0.771	1.767E-02	keV
	kT_{bb}	3.000E-03	frozen	keV
	inp_type	1.000	frozen	0/1
	Redshift	1.000	frozen	
	norm	1.599E-03	1.323E-5	
pexmon	*PhoIndex*	1.823	tied to *(p2)*	
	foldE	1.000	frozen	keV
	rel_refl	-0.242	2.277E-02	
	redshift	1.632E-02	frozen	
	abund	1.000	frozen	
	Fe_abund	1.000	frozen	
	Incl	30.000	frozen	deg
	norm	1.857E-02	1.748E-03	

In *Table B.2* we only report the best-fit values for the main emission components.

Table B.2: Parameters of the best- fit model B of the observation S4

Model	Parameter	Value	Error (+/-)	Unit
TBabs	*nH*	4.105E-02	frozen	$10^{22}\ cm^{-2}$
zashift	*Redshift*	-6.651E-03	frozen	
xillverCp	*gamma*	1.825	3.547E-02	
	Afe	2.399	frozen	
	kTe	17.240	53.2347	keV
	logxi	0.0	frozen	
	z	1.627E-02	frozen	
	Incl	30.000	frozen	deg
	refl_frac	-0.497	3.544E-02	
	norm	1.149E-04	7.299E-05	
xillverCp	*gamma*	1.825	frozen	
	Afe	2.399	frozen	
	kTe	17.240	frozen	keV
	logxi	0.0	frozen	
	z	1.627E-02	frozen	
	Incl	30.000	frozen	deg
	refl_frac	0.0	frozen	
	norm	1.149E-04	7.299E-05	
zgauss	*LineE*	6.700	frozen	keV
	Sigma	0.0	frozen	keV
	Redshift	1.627E-02	frozen	
	norm	6.376E-06	1.685E-06	
gaussian	*LineE*	0.721	frozen	keV
	Sigma	7.242E-02	frozen	keV
	norm	1.338E-04	frozen	
gaussian	*LineE*	0.988	frozen	keV
	Sigma	7.791E-02	frozen	keV
	norm	5.026E-05	frozen	
nthComp	*Gamma*	2.840	3.786E-02	
	kT_e	0.554	0.101	keV
	kT_{bb}	3.068E-03	frozen	keV
	inp_type	1.000	frozen	0/1
	Redshift	1.627E-02	frozen	
	norm	2.591E-03	2.842E-02	
zgauss	*LineE*	6.966	frozen	keV
	Sigma	0.0	frozen	keV
	Redshift	1.627E-02	frozen	
	norm	2.568E-06	frozen	

The parameters of the gaussian have been frozen to the values obtained by [Middei *et al* 2018].